



Comprehensive Analysis of Protein Acetylation and Glucose Metabolism in Mouse Brains Infected with Rabies Virus

Jie Pei,^{a,b} Yueming Yuan,^{a,b} Dayong Tian,^{a,b} Fei Huang,^{a,b} Chengguang Zhang,^{a,b} Caiqian Wang,^{a,b} Ming Zhou,^{a,b} Huanchun Chen,^{a,b} Zhenfang Fu,^{a,b,c} Ling Zhao^{a,b}

^aState Key Laboratory of Agricultural Microbiology, Huazhong Agricultural University, Wuhan, China

^bKey Laboratory of Preventive Veterinary Medicine of Hubei Province, College of Veterinary Medicine, Huazhong Agricultural University, Wuhan, China

^cDepartment of Pathology, University of Georgia, Athens, Georgia, USA

Jie Pei and Yueming Yuan contributed equally to this work. Author order was determined alphabetically.

ABSTRACT Rabies, caused by rabies virus (RABV), is a widespread zoonosis that is nearly 100% fatal. Alteration of the metabolic environment affects viral replication and the immune response during viral infection. In this study, glucose uptake was increased in mouse brains at the late stage of infection with different RABV strains (lab-attenuated CVS strain and wild-type DRV strain). To illustrate the mechanism underlying glucose metabolism alteration, comprehensive analysis of lysine acetylation and target analysis of energy metabolites in mouse brains infected with CVS and DRV strains were performed. A total of 156 acetylated sites and 115 acetylated proteins were identified as significantly different during RABV infection. Compared to CVS- and mock-infected mice, the lysine acetylation levels of glycolysis and tricarboxylic acid (TCA) cycle enzymes were decreased, and enzyme activity was upregulated in DRV-infected mouse brains. Metabolomic analysis revealed high levels of oxaloacetate (OAA) in RABV-infected mouse brains. Specifically, the OAA level in CVS-infected mouse brains was higher than that in DRV-infected mouse brains, which contributed to the enhancement of the metabolic rate at the substrate level. Finally, we confirmed that OAA could reduce excessive neuroinflammation in CVS-infected mouse brains by inhibiting JNK and P38 phosphorylation. Taken together, this study provides fresh insight into the different strategies the host adapts to regulate glucose metabolism for energy requirements after different RABV strain infections and suggests that OAA treatment is a strategy to prevent neural damage during RABV infection.

IMPORTANCE Both viral replication and the host immune response are highly energy dependent. It is important to understand how the rabies virus affects energy metabolism in the brain. Glucose is the direct energy source for cell metabolism. Previous studies have revealed that there is some association between acetylation and metabolic processes. In this study, comprehensive protein acetylation and glucose metabolism analysis were conducted to compare glucose metabolism in mouse brains infected with different RABV strains. Our study demonstrates that the regulation of enzyme activity by acetylation and OAA accumulation at the substrate level are two strategies for the host to respond to energy requirements after RABV infection. Our study also indicates the role OAA could play in neuronal protection by suppressing excessive neuroinflammation.

KEYWORDS rabies virus, acetylation, glucose, metabolites, oxaloacetate, inflammation

Rabies is a widespread fatal zoonosis with a mortality rate of nearly 100% after clinical symptoms have developed (1). Rabies virus (RABV) is the causative agent of rabies, and it causes serious damage to the host central nervous system (CNS) (2, 3). There are no effective antiviral drugs against RABV. Proteomic analysis has revealed several metabolic enzyme changes during RABV infection, indicating the pivotal role

Editor Rebecca Ellis Dutch, University of Kentucky College of Medicine

Copyright © 2022 American Society for Microbiology. All Rights Reserved.

Address correspondence to Ling Zhao, zling604@yahoo.com.

The authors declare no conflict of interest.

Received 10 November 2021

Accepted 3 December 2021

Accepted manuscript posted online 8 December 2021

Published 23 February 2022

metabolism plays in rabies (4–7). Metabolomic analysis of human cerebrospinal fluid and mouse brain tissues has further clarified the metabolic abnormalities induced by RABV (1, 8).

However, the metabolic enzymes identified in early proteomic studies (i.e., isoform alpha-enolase, glutamine synthetase, NADH dehydrogenase, etc.) (5, 9) are not sufficient to account for the metabolic flux changes that occur after RABV infection. Hundreds of posttranslational modifications (PTMs) enrich the diversity of protein functions. Lysine acetylation is a key PTM in cellular regulation, and many enzymes that participate in intermediate metabolism are acetylated (10). Numerous studies have identified the role of acetylation in the regulation of enzyme subcellular location, activity, and stability during various metabolic processes. Almost all enzymes involved in glycolysis, gluconeogenesis, the tricarboxylic acid (TCA) cycle, the urea cycle, fatty acid metabolism, and glycogen metabolism are acetylated (11). Acetyl-coenzyme A (CoA) is the primary acetyl donor for protein acetylation. In addition, acetyl-CoA is the central substrate for the TCA cycle. The dual role of acetyl-CoA suggests a link between acetylation and metabolic regulation.

Oxaloacetate (OAA) is an important metabolic intermediate that is condensed with acetyl-CoA to form citric acid, which is the first step of the TCA cycle in mitochondria. The oxidation of OAA to malate converts NADH to NAD⁺, which may also enhance glycolysis flux and increase mitochondrial mass (12, 13). Treatment with OAA in a mouse model enhances the bioenergetic infrastructure and induces insulin signaling in mouse brains (14). Recent studies have revealed the pharmacology of OAA in traumatic brain injury, ischemia, and some neurodegenerative diseases (14–18). These studies have confirmed that OAA confers neuroprotection by scavenging glutamate, reducing inflammation, and stimulating neurogenesis in the brain. Another study reported that OAA is hepatoprotective because it inhibits the mitogen-activated protein kinase (MAPK) pathway and mitochondrial apoptosis (19).

In this study, brain tissues from lab-attenuated RABV strain CVS- and wild-type RABV strain DRV-infected mice were harvested for proteomic analysis of protein acetylation. We found that the brains of RABV-infected mice exhibited dramatic changes in metabolic enzyme acetylation. To further confirm the status of metabolites involved in glucose metabolism, target energy metabolite analysis was conducted, and abnormal OAA accumulation was observed in the mouse brains at the late stage of RABV infection. Further, OAA treatment reduced neuroinflammation at the late stage of CVS infection by inhibiting JNK and P38 signaling pathways.

RESULTS

RABV infection elevates glucose requirements in mouse brains. Both viral replication and host immune response are highly energy dependent. To investigate the effect of RABV infection on energy metabolism in a mouse model, groups of 6-week-old female C57BL/6 mice ($n = 4$) were intracranially (i.c.) inoculated with 200 focus-forming units (FFU) of CVS, DRV, or Dulbecco's modified Eagle's medium (DMEM) (all with the same volume). At 7 days postinfection (dpi), the mouse brains were harvested, homogenized, and then subjected to glucose content analysis by using a commercial glucose content detection kit. A higher level of glucose was observed in the brains of CVS-infected and DRV-infected mice than in the brains of mock-infected mice (Fig. 1A). Since GLUT1 is the major glucose transporter in the blood-brain barrier (BBB) and plays a key role in maintaining the stability of brain energy supply, its content in mouse brains was also measured. Both the mRNA (Fig. 1B) and protein (Fig. 1C) levels of GLUT1 were upregulated in the brain of CVS-infected and DRV-infected mice compared with the brains of mock-infected mice. These results indicate that RABV infection promotes glucose uptake in mouse brains.

CVS and DRV infection cause differential protein acetylation profiles in mouse brains. Acetylation is one of the major PTMs that is strongly interlinked with glucose metabolism, so we performed liquid chromatography–mass spectrometry (LC-MS) to detect acetylated proteins in RABV-infected mouse brains and explore the detailed

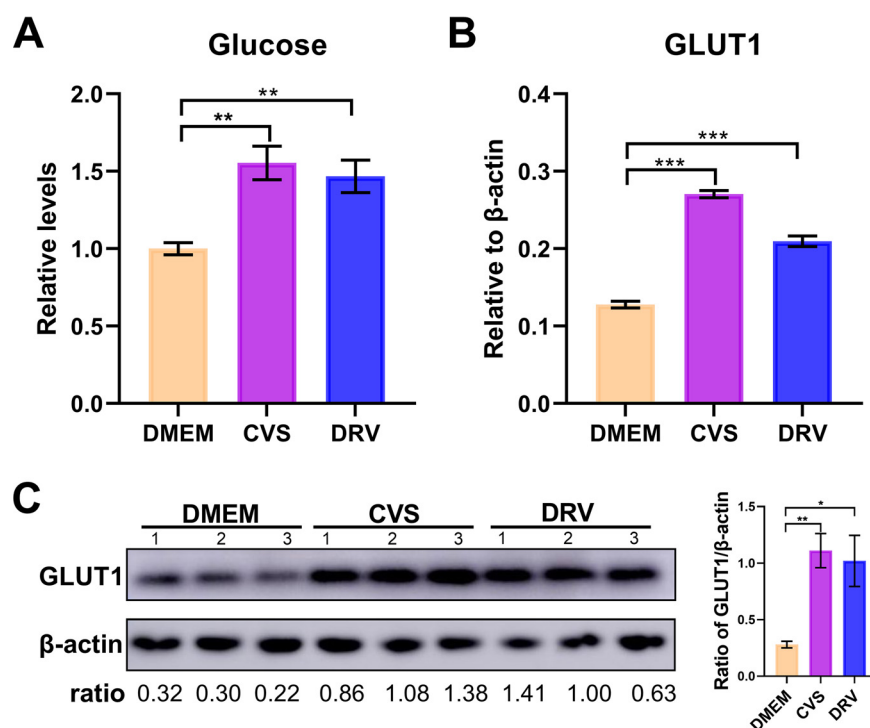


FIG 1 CVS and DRV infections increase glucose in the mouse brain. C57BL/6 mice ($n = 4$) were intracerebrally (i.c.) inoculated with CVS, DRV (200 FFU/mouse), or DMEM, and the brains were harvested at 7 dpi to analyze the glucose levels and gene expression. (A) The concentration of glucose in the mouse brain was analyzed using a glucose content detection kit ($n = 4$). (B and C) The mRNA level of GLUT1 in the mouse brain ($n = 4$) was quantified by qPCR, and the protein level of GLUT1 was analyzed by Western blotting. The results are presented as the mean \pm standard error of the mean (SEM). Asterisks indicate P values compared with the control: *, $P < 0.05$; **, $P < 0.01$; ***, $P < 0.001$.

mechanism of how RABV infection promotes glucose uptake. To reveal the changes in lysine acetylation due to RABV infection, the mouse brains infected with different RABV strains were harvested for a quantitative proteomic assay (Fig. 2A). To avoid inconsistent proteomic analysis results caused by different virus strains, first the viral load in the mouse brains infected with CVS and DRV was balanced. According to our previous study (20), CVS- and DRV-infected mice were sacrificed at 7 dpi, and the brains were harvested. Virus genomic RNA (vRNA) level (Fig. 2B) and protein level of RABV-N (Fig. 2C) both confirmed that the viral loads in mouse brains infected with CVS and DRV were comparable at 7 dpi.

To investigate protein acetylation changes in mouse brains infected with different RABV strains, the mouse brains mentioned above were subjected to LC-MS/MS analysis in triplicates. A total of 1,062 lysine acetylation sites in 540 proteins were identified, among which 898 sites in 460 proteins with statistical significance of the acetylation level were chosen for further analysis. Of these proteins, 156 sites in 115 proteins displayed significant differences (quantitative ratio over 1.5 or below 1 to 1.5; $P < 0.05$) in lysine acetylation levels between DRV-infected and mock-infected brains (40 sites of 34 proteins were upregulated and 116 sites of 87 proteins were downregulated), 7 sites in 7 proteins displayed significant differences in lysine acetylation levels between CVS-infected and mock-infected brains (7 sites of 7 proteins were upregulated), and 173 sites in 125 proteins displayed significant differences in acetylation levels between DRV-infected and CVS-infected brains (35 sites of 32 proteins were upregulated and 138 sites of 100 proteins were downregulated).

The differentially acetylated proteins were then further characterized. Many of the upregulated and downregulated proteins in the DRV- versus CVS-infected comparison group overlapped the upregulated proteins (21/32, 65.6%) and downregulated

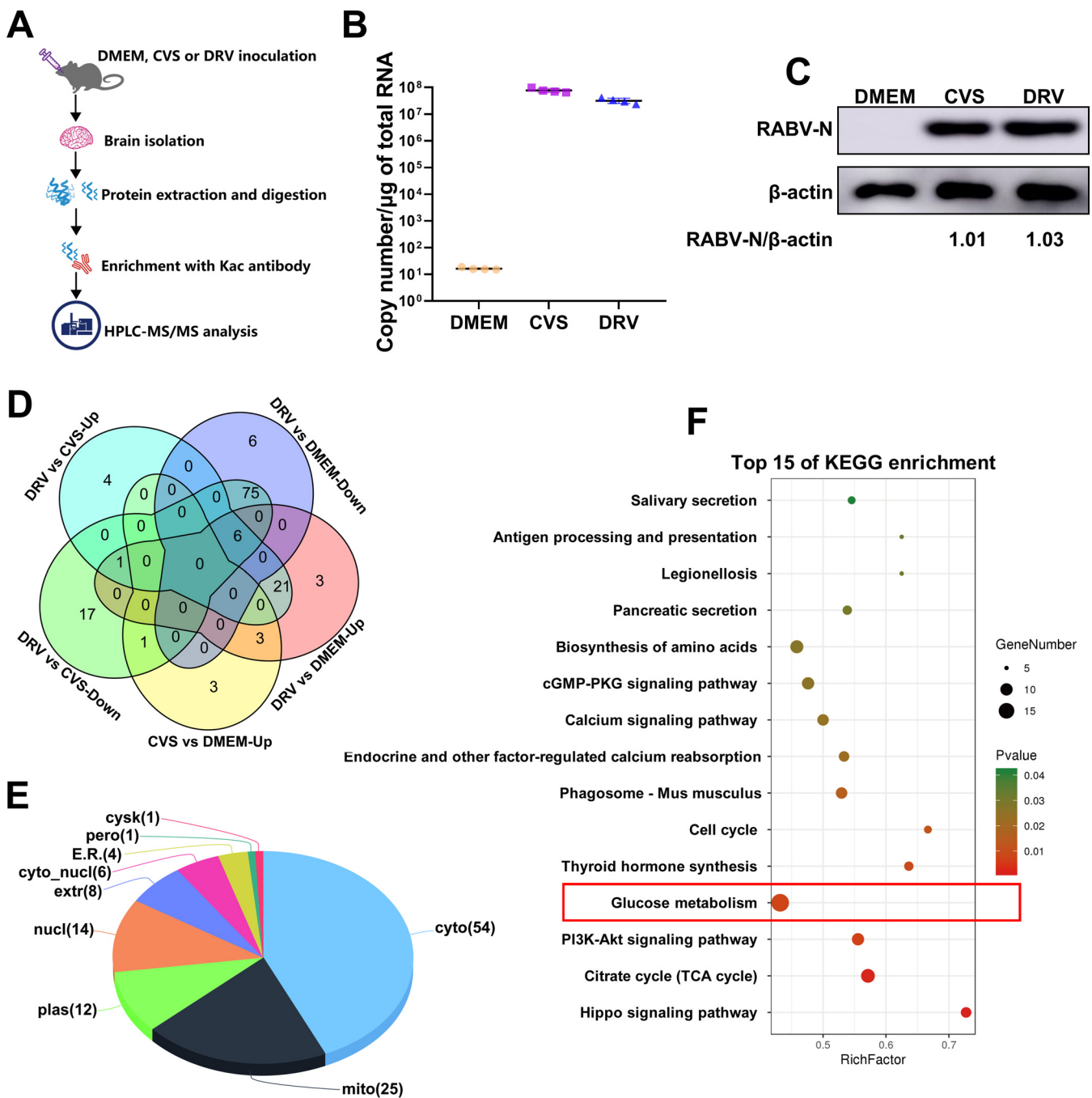


FIG 2 Comparative analysis of protein acetylation of DMEM-, CVS-, and DRV-infected mouse brains. C57BL/6 mice ($n = 3$) were i.c. inoculated with CVS, DRV (200 FFU/mouse), or DMEM, and the brains were harvested at 7 dpi for the analysis of protein acetylation. (A) A workflow schematic is shown to depict how lysine acetylation was identified. (B) Viral copy numbers ($n = 4$) were quantified by qPCR and compared. (C) The RABV-N protein level was analyzed by Western blotting. (D) The Venn diagram shows the upregulated proteins in the CVS- versus DMEM-infected comparison group and the upregulated and downregulated proteins in the DRV- versus CVS-infected and DRV- versus DMEM-infected comparison groups. (E) A pie chart compares the subcellular location of different proteins in the CVS- and DRV-infected comparison groups ($P < 0.05$). (F) KEGG pathway enrichment analysis is shown in a bubble chart. Bubble map and Venn diagram analyses were performed using the OmicShare tool. P values were calculated using Benjamini-corrected modified Fisher's exact test.

proteins (75/100, 75%) in the DRV- versus DMEM-infected comparison group (Fig. 2D). The differentially acetylated proteins in the DRV- versus CVS-infected group were mostly distributed in the cytoplasm (54/125, 43.2%) and mitochondria (25/125, 20%) (Fig. 2E). To evaluate potential biological functional differences caused by the two different RABV strains, the differentially acetylated proteins in the DRV- versus CVS-

infected group were analyzed by Kyoto Encyclopedia of Genes and Genomes (KEGG) pathway enrichment, and the result showed that the differences in glucose metabolism pathways rank 1st among the top 15 enrichments, with the number of differential proteins being more than 15 and the *P* value being less than 0.01 (Fig. 2F). Together, these results demonstrate that the acetylation level of proteins involved in glucose metabolism was altered in DRV-infected mouse brains.

The acetylation level of glucose metabolism enzymes was downregulated in DRV-infected mouse brains. Almost all enzymes involved in glycolysis and the TCA cycle are acetylated, and numerous acetylated lysine sites and their functions have been identified. Our results identified that during DRV infection, the acetylation level of many proteins involved in glycolysis and the TCA cycle was changed (Fig. 3A). The acetylation level of nearly all glycolysis enzymes (HK1, PKF, TPI1, glyceraldehyde-3-phosphate dehydrogenase [GAPDH], PGK1, ENO, and LDHb) was downregulated with DRV infection (Fig. 3B). The acetylation level of TCA cycle enzymes fluctuated. The acetylation level of pyruvate dehydrogenase (PDH), Aconitate hydratase (ACO), 2-oxoglutarate dehydrogenase (OGDH), and dihydrolipoyllysine-residue acetyltransferase component of pyruvate dehydrogenase complex (DLAT) was downregulated with DRV infection, while some lysine sites displayed an upregulated trend (such as k272 of IDH2, k223 of IDH3a, k574 of SDHb, k97 of FH, and k296 of MDH2) (Fig. 3C). The highly downregulated acetylated proteins GAPDH, PDH1 α , and MDH1 were selected, and their acetylation sites and acetylation levels, analyzed by LC-MS, are shown (Fig. 3D to F). The acetylated proteins described above were enriched by using immunoprecipitation and then confirmed by Western blotting (Fig. 3G to I).

Glucose metabolism enzyme activity was enhanced in DRV-infected mouse brains. Several previous studies indicated that lysine acetylation of enzymes at specific sites could regulate enzyme activity (11, 21–23). Thus, we further investigated the activity of glucose metabolism enzymes in RABV-infected brains using commercial enzyme activity detection kits. The results indicated that the activity of hexokinase (HK), GAPDH, PDH, isocitrate dehydrogenase (IDH), succinate dehydrogenase (SDH), and malate dehydrogenase (MDH), which are involved in the TCA cycle, in the DRV-infected group was significantly increased compared to that in the CVS-infected groups (Fig. 4A to H).

Oxaloacetate accumulates in mouse brains at the late stage of RABV infection. To further explore the energy metabolic environment in RABV-infected brains, metabolic profiling of target energy metabolites was performed with multiple-reaction monitoring (MRM). Although the activity of glycolysis and TCA cycle enzymes in DRV-infected mouse brains was higher than that in CVS-infected mouse brains, the metabolite content was comparable between CVS- and DRV-infected mouse brains (Fig. 5A). Surprisingly, oxaloacetate, which is generated in the first step of the TCA cycle, accumulated at a high level in CVS-infected mouse brains. The oxaloacetate level in the brains of CVS-infected mice was 4.2-fold higher than that in DRV-infected mouse brains (Fig. 5B).

CVS induces stronger inflammation in the mouse brain than DRV. Several previous studies have shown that lab-attenuated RABV causes activation of the host immune response, while wild-type RABV can evade it (20, 24–26). To further confirm these findings, we compared the inflammation caused by CVS and DRV infection in the mouse brain. The immunohistochemistry (IHC) analysis showed that CVS induced much stronger inflammatory responses in mouse brains than DRV (Fig. 6A). To specify the cell types that caused the obvious neuroinflammation by CVS, we homogenized the mouse brains at 7 dpi, and leukocytes were isolated and analyzed by flow cytometry. Several cell types infiltrated into CVS-infected mouse brains were observed, including neutrophils (CD45^{hi} Ly6G⁺), T cells (CD45⁺ CD3⁺), B cells (CD11c[–] CD45⁺ B220⁺), and macrophages (CD45^{hi} CD11b⁺) (Fig. 6B to E). A previous study demonstrated that microglia (CD45 intermediate) could be distinguished from macrophages (CD45^{hi} cells) (27). Following this strategy, we first gated on the CD45^{int} cells and then reanalyzed them (CD45^{int}) by introducing two markers, CD11b and TMEM119, of which TMEM119 is a specific marker for microglia. The results showed that significantly more microglia

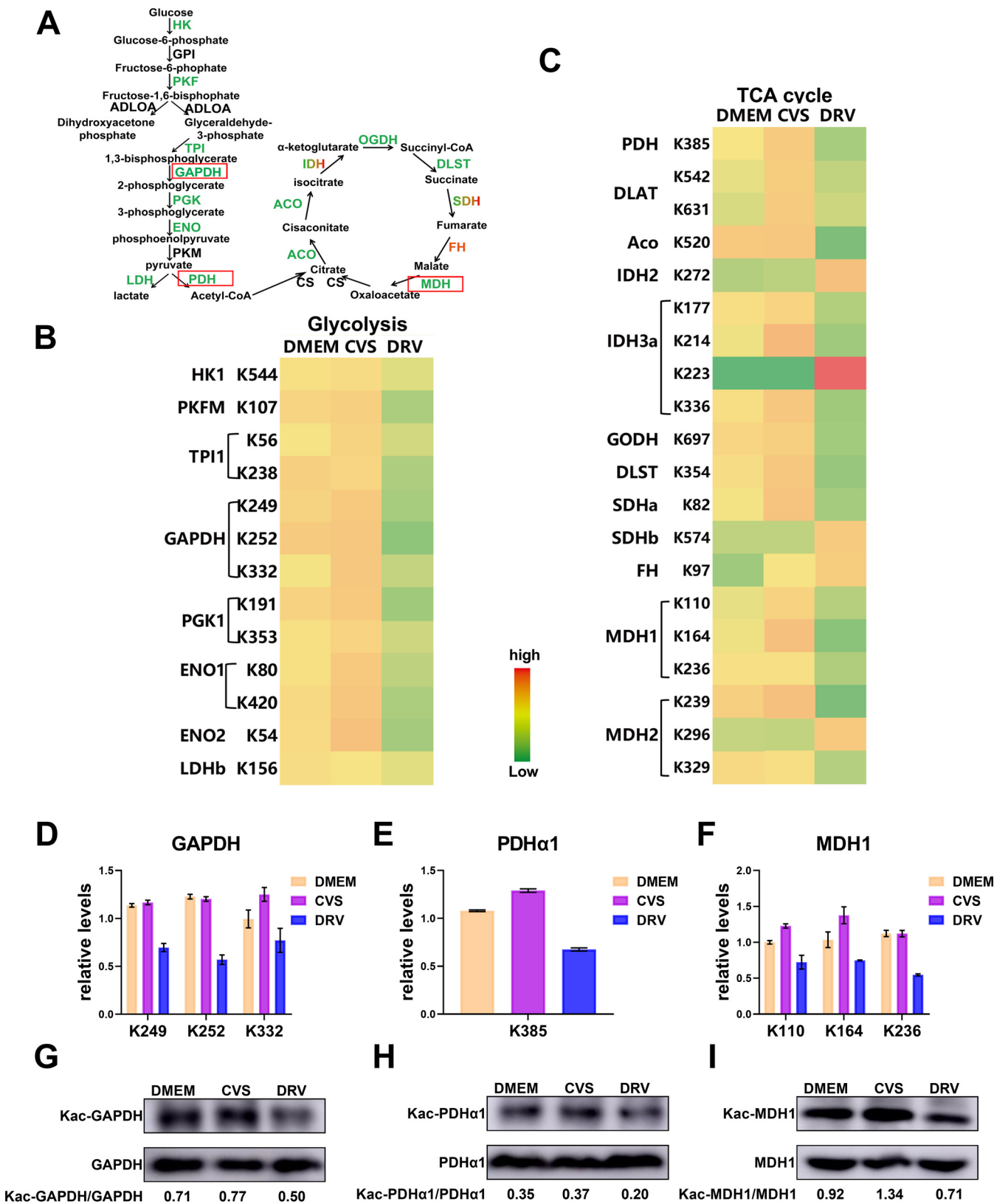


FIG 3 Comparative analysis of enzyme acetylation in the glucose metabolic pathway. (A) A schematic is shown of glycolysis and the TCA cycle of the glucose metabolic pathway. Detailed information on the acetylation sites was further extracted. (B and C) A heat map shows the different acetylation sites of the enzymes involved in glycolysis (B) and the TCA cycle (C) identified when comparing CVS-, DRV-, or DMEM-infected mice ($n = 3$). (D to F) The normalized level of acetylation at specific sites in GAPDH (D), PDH α (E), and MDH1 (F) was compared. (G to I) The acetylation levels of GAPDH (G), PDH α (H), and MDH1 (I) in the mouse brain were analyzed by Western blotting.

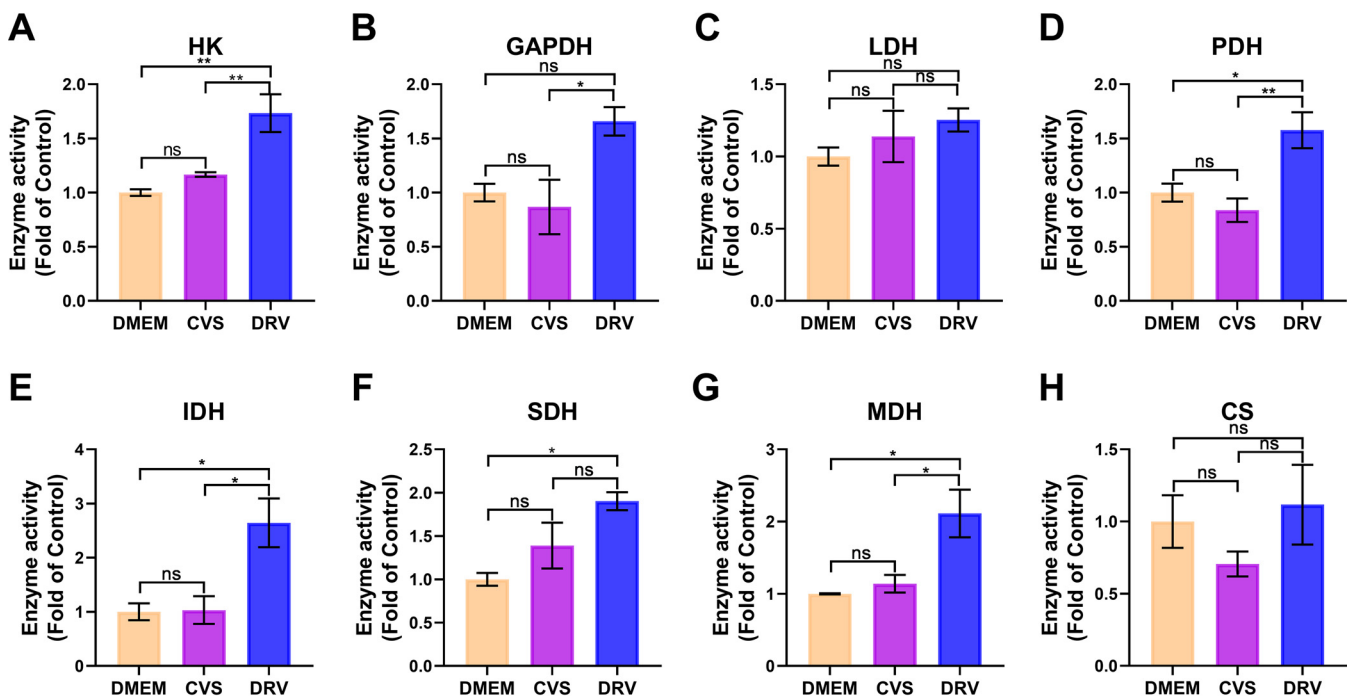


FIG 4 Comparative analysis of enzyme activity in the glucose metabolic pathway. C57BL/6 mice ($n = 5$) were i.c. inoculated with CVS, DRV (200 FFU/mouse), or DMEM, and the brains were harvested at 7 dpi to assess enzyme activity. (A to H) Graphs of the enzyme activity of hexokinase (HK), glyceraldehyde-3-phosphate dehydrogenase (GAPDH), lactate dehydrogenase (LDH), pyruvate dehydrogenase (PDH), citrate synthase (CS), isocitrate dehydrogenase (IDH), succinate dehydrogenase (SDH), and malate dehydrogenase (MDH) ($n = 4$ to 5) in mouse brains inoculated with CVS, DRV, or DMEM are shown. The results are presented as the mean \pm SEM. Asterisks indicate P values compared with the control: *, $P < 0.05$; **, $P < 0.01$.

were present in the CVS-infected mouse brains than those in the mock-infected mouse brains (Fig. 6F). Furthermore, a pie graph was created and indicated that infiltrated macrophages (83.39%) took on greater responsibility on the upregulation of inflammatory response than microglia (16.61%) in CVS-infected mouse brains (Fig. 6G). Taken together, these results demonstrate that CVS infection induces more neuroinflammation and immune cell infiltration than DRV infection in mouse brains.

OAA treatment reduces excessive neuroinflammation *in vivo*. The level of neuroinflammation was consistent with the accumulation of OAA in the mouse brains infected with different RABV strains, indicating the role of OAA in suppressing virus-induced inflammation. To confirm this hypothesis, CVS-infected mice were intraperitoneally injected with 1 g/kg of body weight/day OAA for 7 days, and the brains were harvested for inflammation evaluation. Western blot analysis revealed that the phosphorylation of JNK and P38 was increased in CVS-infected mouse brains (Fig. 7A). However, with OAA treatment, although the RABV-N protein level was not changed, the activation of both JNK and P38 was downregulated. In addition, consistent with the Western blotting results, real-time quantitative PCR (qPCR) results (Fig. 7B) showed that although the viral load was not affected, the mRNA levels of tumor necrosis factor alpha (TNF- α), CCL2, and CXCL10 were reduced after OAA treatment. The number of CD45⁺ cells in the cerebrum, cerebellum, and hippocampus was also significantly reduced after treatment with OAA at the late stage of CVS infection (Fig. 7C). These results indicate that OAA can suppress excessive neuroinflammation in the brains of CVS-infected mice.

DISCUSSION

RABV replication and the host immune response are both highly energy dependent (28–30). The high energy demand of neurons is mainly supplied by glucose, which is accomplished by glucose transporters in capillaries and brain cells (31). Translocation across the blood-brain barrier (BBB) of glucose is mainly mediated by high-affinity glucose

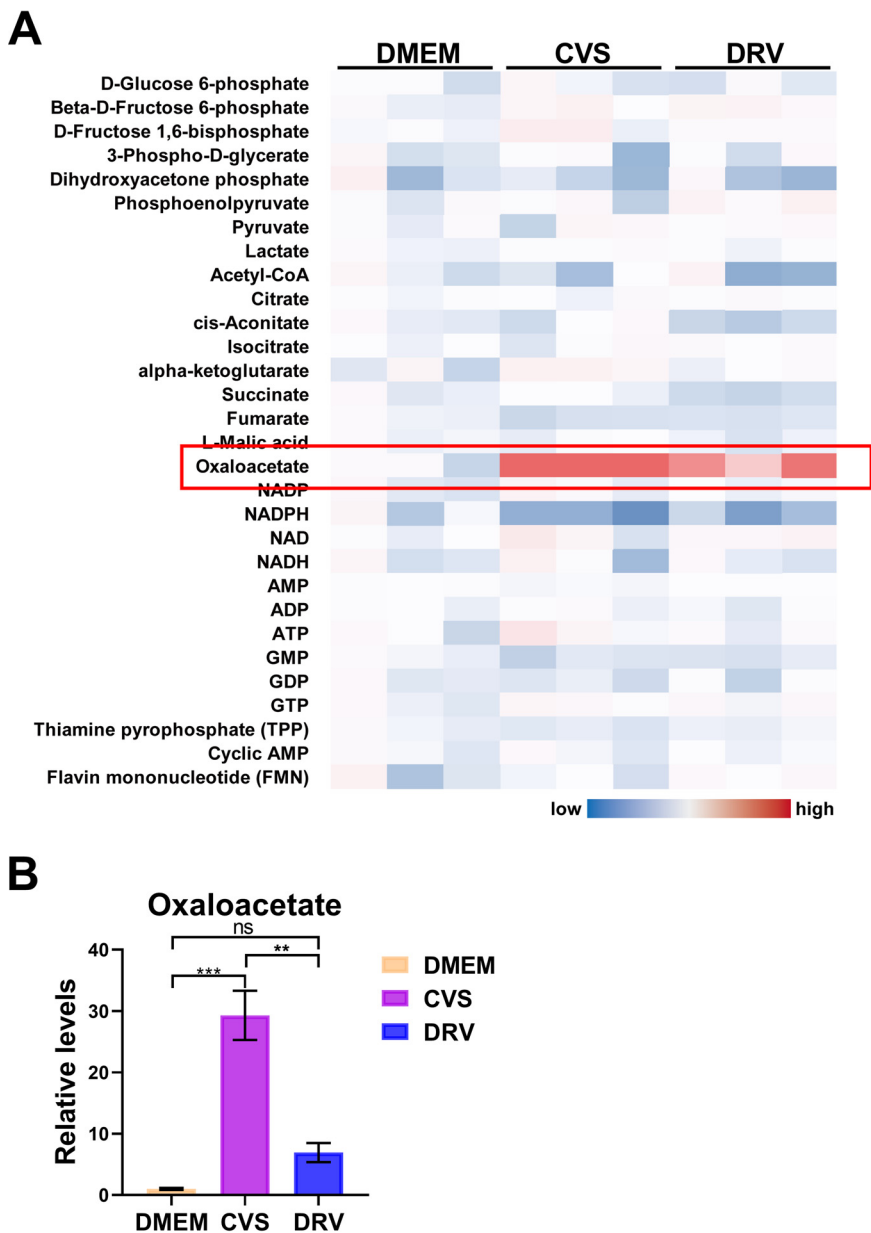


FIG 5 Comparative analysis of energy metabolism. C57BL/6 mice ($n = 3$) were i.c. inoculated with CVS, DRV (200 FFU/mouse), or DMEM, and the brains were harvested at 7 dpi for glucose metabolism analysis. (A) A heat map depicts energy metabolism in the mouse brain. (B) The oxaloacetate level is compared in the brains of CVS-, DRV-, or DMEM-infected mice ($n = 3$). The results are presented as the mean \pm SEM. Asterisks indicate P values compared with the control: *, $P < 0.05$; **, $P < 0.01$; ***, $P < 0.001$.

transporter type 1 (GLUT1) (32). The glucose upregulation observed in the brains of RABV-infected mice here is consistent with a previous study (8). Further, we also revealed an up-regulation of GLUT1 expression, indicating an increase in glucose uptake rather than a decrease in glucose utilization in the brains of RABV-infected mice.

Proteomic analysis of protein expression *in vitro* and *in vivo* was conducted in previous studies to explore the pathogenic mechanisms of different RABV strains (4–7). However, the few identified differently expressed proteins were not sufficient to explain such a complicated biological process. PTMs are dynamic and can precisely regulate the physical and chemical properties, conformations, and functions of proteins (33). Among the different regulatory processes, PTMs occur at a much higher rate

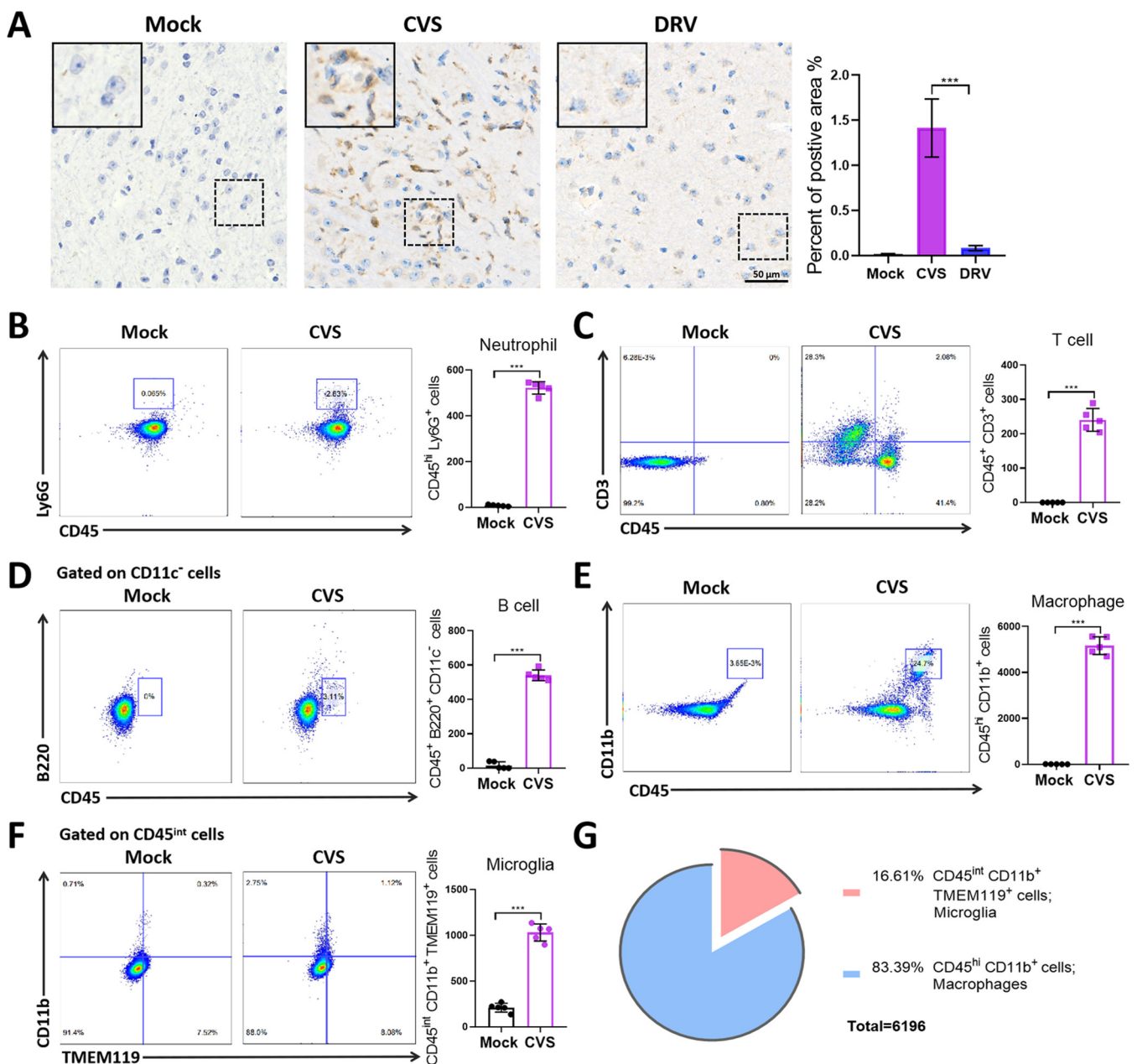


FIG 6 CVS infection induces neuroinflammation and immune cell infiltration in mouse brains. Mice ($n = 5$) were i.c. infected with CVS (200 FFU/mouse), and brains were harvested at 7 dpi. Mouse brains were prepared into paraffin sections, and CD45⁺ cells were stained by immunohistochemistry. (A) Representative immunohistochemistry stained with anti-CD45 antibody. The quantity of CD45-positive cells was calculated by using ImageJ. (B to F) Mouse brains were homogenized, and leukocytes were isolated for analysis of neutrophils (CD45^{hi} Ly6G⁺), T cells (CD45⁺ CD3⁺), B cells (CD11c⁻ CD45⁺ B220⁺), macrophages (CD45^{hi} CD11b⁺), and microglia (CD45^{int} CD11b⁺ TMEM119⁺) by flow cytometry. A total of 20,000 events were acquired to generate graphs ($n = 5$). (G) Pie graph showing the proportion of microglia and macrophages in CVS-infected mouse brains. The results are presented as the mean \pm SEM. Asterisks indicate P values compared with the control: *, $P < 0.05$; **, $P < 0.01$; ***, $P < 0.001$. Scale bar, 50 μ m.

with a lower energy cost than protein turnover. In this study, acetylation was analyzed in the brains of mice infected with different RABV strains (attenuated strain CVS and wild-type strain DRV). Altogether, 156 sites in 115 proteins in the brains of DRV-infected mice and 7 sites in 7 proteins in the brains of CVS-infected mice displayed significant differences compared with the proteins in the brains of mock-infected mice. Previous studies revealed that lysine acetylation is a prevalent modification in enzymes involved in metabolic flux (10). The CVS strain, which induced an intense inflammatory response and damage in the brain, resulted in fewer acetylation alterations than the DRV strain, which can evade the immune response in the brain. Thus, we speculated

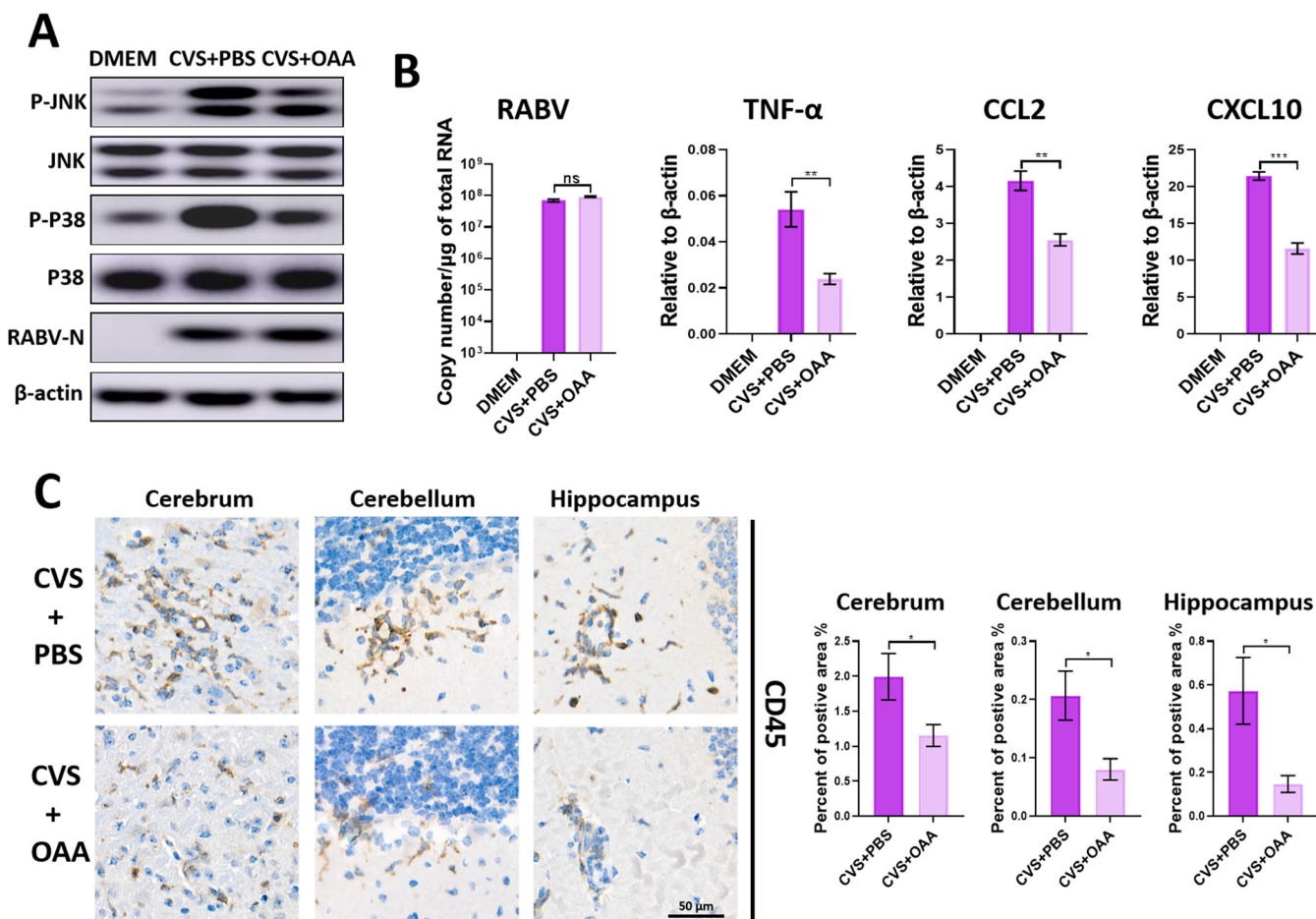


FIG 7 Effects of OAA treatment on neuroinflammation *in vivo*. C57BL/6 mice ($n = 5$) were infected with CVS (200 FFU/mouse) and mock treated with PBS or infected with CVS and treated with OAA for 7 days, and then brain tissues were harvested. (A) Western blot analysis was conducted to assess the levels of P-JNK, total JNK, P-P38, total P38, RABV-N, and β -actin. (B) Quantitative analysis of viral genomic RNA, TNF- α , CCL2, and CXCL10 ($n = 5$) transcripts was conducted by qPCR. (C) Representative images and statistical analysis results (10 random sections from each brain region were selected for calculation) are shown of the CD45⁺ areas in the mouse cerebrum, cerebellum, and hippocampus. The immunohistochemistry (IHC) graphs were analyzed with the IHC profile plugins of ImageJ. The results are presented as the mean \pm SEM. Asterisks indicate P values compared with the control: *, $P < 0.05$; **, $P < 0.01$; ***, $P < 0.001$. Scale bar, 50 μ m.

that the regulation of acetylation is an autoregulation mechanism that the host adapts to meet the changing energy demands in DRV-infected brains, which may also contribute to immune evasion by the DRV strain.

Nearly all glycolysis and TCA cycle enzymes are acetylated (11). With calorie restriction, the acetylation of a vast majority of metabolic enzymes is increased in mouse liver mitochondria, and only a limited number of acetyltransferases and deacetylases are involved in the regulation of numerous metabolic enzymes. Thus, the large acetylation alteration could be caused by a nonenzymatic reaction due to metabolites, such as acetyl-CoA (34). In our research, at the late stage of DRV infection, all discrepant acetylation sites in the glycolysis process and most of the acetylation sites in the TCA cycle presented a downregulation trend, while the expression of deacetylases (histone deacetylases and SIRT1) was not increased (data not shown). Corresponding with the observed acetylation changes, the activity of glucose metabolism enzymes was upregulated in the brains of DRV-infected mice. The acetylation sites identified in our study may regulate enzymes by multiple mechanisms, including enzymatic activation or inhibition, influencing protein stability, or altering subcellular localization (11). Glyceraldehyde 3-phosphate dehydrogenase (GAPDH) is a core glycolysis enzyme. It was reported that acetylation at 251K of human GAPDH (homologous to 249K of mouse GAPDH) regulates its nuclear translocation (35) and that acetylation at 254K (homologous to 252K of mouse GAPDH) increases enzyme activity (21). The

acetylation level of both sites was significantly downregulated in the brains of DRV-infected mice; thus, we presume that deacetylation of 249K increases GAPDH in the cytoplasm to increase enzyme activity, while deacetylation of 249K is inhibitory, leading to a 1.5-fold increase in enzyme activity overall. However, the exact roles of most acetylation sites identified here have not been reported and require further investigation.

Acetylation alteration could be a strategy that DRV-infected mice adapt to increased energy metabolism requirements. We further investigated glucose metabolism in the brains of mice infected with different RABV strains and found that most of the energy metabolites were homeostatic, except oxaloacetate, which was highly increased in mouse brains infected with CVS and DRV (increased by 29.3- and 6.9-fold, respectively, compared to the control). A previous study of glucose metabolism in mice infected with the wild-type RABV strain DOG4 implied that glucose metabolism increased in the brain without significantly changing the level of other carbon metabolites (i.e., lactate, citrate, succinate, fumarate, and malate) (8). However, in a different study, carbon metabolites (lactate, succinate, and malate) were significantly increased in the cerebrospinal fluid of rabid humans (1). Combining these two studies, we assume that the excess carbon metabolites are carried away by cerebrospinal fluid to maintain homeostasis in RABV-infected brains. Notably, abnormal accumulation of oxaloacetate was observed in the brains of RABV-infected mice. OAA is the core intermediate metabolite that condenses with acetyl-CoA in the first step of the TCA cycle. The increase in OAA at the substrate level could enhance energy metabolism by promoting glycolysis and accelerating respiration rates (17). The oxidation of OAA to malate converts NADH to NAD⁺, which also accelerates glycolysis flux and increases mitochondrial mass (12, 13). Thus, the accumulation of OAA in mouse brains might be the main strategy adapted by CVS-infected mice to enhance energy metabolism.

In the last decade, the pharmacology of OAA has raised attention. The abundant accumulation of OAA in the brains of RABV-infected mice reminds us that OAA could be used for the treatment of RABV infection. OAA was once administered to patients in capsule form for the treatment of Alzheimer's disease (AD) in a preclinical study (36). Apart from AD, recent studies have also tested the possibility of using OAA to treat traumatic brain injury, stroke, amyotrophic lateral sclerosis, and seizures (14–18, 37). OAA treatment activates mitochondrial biogenesis, stimulates neurogenesis, and reduces inflammation in mouse brains. OAA could also serve as a glutamate or reactive oxygen species (ROS) scavenger to provide neuroprotection. During RABV infection, glutamate release is enhanced in human cerebrospinal fluid (1), and glutamate ammonia ligase is upregulated in mouse brains (9). It was also reported that RABV phosphoprotein induces ROS production (38–40). A recent study revealed the role of OAA in inhibiting the MAPK pathway in chemical liver injury (19). It was also reported that different RABV strains activate the MAPK pathway to various degrees at the late stage of virus infection, and laboratory-attenuated strains induce a much higher level of MAPK phosphorylation than wild-type strains (41). A recent study revealed that the inflammatory response and MAPK signaling pathway activation are stronger during natural infection in dogs and humans than with artificial infection in mouse models (42). The wild-type DRV strain in our study induced slight inflammation in the mouse model, which prevented quantitative analysis of the inflammatory response. While the CVS strain induced a strong inflammatory response, CVS-infected mice were treated with OAA to further explore the anti-inflammatory effect of OAA in mouse brains. Although OAA treatment did not suppress viral replication in mouse brains, in accordance with the role of OAA in inhibiting the MAPK pathway in chemical liver injury, the activation of JNK and P38 signaling in the MAPK pathway was obviously inhibited by OAA after CVS infection, resulting in a reduction in inflammation in the cerebrum, cerebellum, and hippocampus of mouse brains. Thus, we suppose that the upregulation of OAA in CVS-infected mouse brains is due to the stronger inflammatory response compared with that in DRV-infected mouse brains, which is a feedback regulation mechanism.

In summary, comprehensive lysine acetylation proteomic analysis and target energy metabolite analysis in brains infected with different RABVs were conducted in this study. The results indicate that during RABV infection, the host brain has high energy

demands and the uptake of glucose is enhanced. Different strategies are adapted by the host to respond to the glucose metabolism requirements following infection by different RABV strains. Abundant OAA accumulation in the brains of CVS-infected mice may increase the metabolic rate at the substrate level. In addition to the accumulation of OAA, the enzyme activity of glucose metabolic enzymes is also enhanced by the alteration of the enzyme acetylation level in the brains of DRV-infected mice. OAA may contribute to the reduction of inflammation and provide neuroprotection for mouse brains during CVS infection.

MATERIALS AND METHODS

Viruses, cells, antibodies, kits, and mice. Lab-attenuated RABV strain CVS-B2c (CVS) (43, 44) and wild-type strain DRV-AH08 (DRV) (isolated from a rabid dog in Anhui Province, China, in 2008) were kept in our laboratory (45, 46). N2a (neuroblastoma) cells were cultured in Dulbecco's modified Eagle's medium (DMEM) (Thermo-Fisher, USA) supplemented with 10% fetal bovine serum (FBS) (Thermo-Fisher). For mouse infection, both CVS and DRV were propagated in suckling ICR mouse brains. Both viruses were manipulated according to standard biosecurity procedures of the Ministry of Agriculture of China.

The anti-RABV-N mouse monoclonal antibody was prepared in our laboratory. The anti-Kac mouse monoclonal antibody was purchased from PTM-BIO (Hangzhou, China). Anti- β -actin, anti-GLUT1, and anti-GAPDH mouse monoclonal antibodies and anti-PDH1 α and anti-MDH1 rabbit polyclonal antibodies were purchased from ProteinTech (Wuhan, China). Anti-JNK, anti-phospho-JNK (P-JNK), anti-P38, and anti-phospho-P38 (P-P38) rabbit monoclonal antibodies were purchased from Cell Signaling Technology (MA, USA). Horseradish peroxidase (HRP)-conjugated secondary antibodies were purchased from Boster Biotech (Wuhan, China).

Kits for quantification of glucose and for determining enzyme activity of hexokinase (HK), glyceraldehyde-3-phosphate dehydrogenase (GAPDH), lactate dehydrogenase (LDH), pyruvate dehydrogenase (PDH), citrate synthase (CS), isocitrate dehydrogenase (IDH), succinate dehydrogenase (SDH), and malate dehydrogenase (MDH) were purchased from Solarbio (Beijing, China).

Six-week-old female C57BL/6 mice were purchased from the Center for Disease Control and Prevention of Hubei Province in Wuhan, China. All animal experiments were approved by the Scientific Ethics Committee of Huazhong Agricultural University with permit number HZAUMO-2017-010 and conducted in strict accordance with the recommendations in the Guide for the Care and Use of Laboratory Animals of the Ministry of Science and Technology of China.

Mouse infection. Six-week-old female C57BL/6 mice were intracerebrally (i.c.) inoculated with 200 focus-forming units (FFU) of CVS-, DRV-, or mock-infected DMEM. At 7 days postinfection (dpi), the mice exhibited severe paralysis and were anesthetized with ketamine-xylazine and perfused by intracardiac injection with phosphate-buffered saline (PBS) before the brain tissues were harvested. The brain tissues were ground with liquid nitrogen for protein analysis or were fixed in 4% paraformaldehyde for immunohistochemistry analysis.

Glucose quantification in mouse brains. The glucose content detection kit (Solarbio, Beijing, China) is based on the theory that glucose oxidase catalyzes the oxidation of glucose to gluconic acid and produces hydrogen peroxide, and peroxidase catalyzes hydrogen peroxide to oxidize 4-aminoantipyrine linophenol to produce colored compounds with characteristic absorption peaks at 505 nm. Brain tissues (0.1 g) were extracted in 1 ml of sterile water and homogenized with ultrasonication. The tissues then were placed in a water bath at 95°C for 10 min. After cooling to room temperature, the samples were centrifuged at $8,000 \times g$ for 10 min, and the glucose concentration of the supernatant was determined using the glucose content detection kit.

LC-MS/MS analysis of lysine acetylation in mouse brains. Brain tissues were homogenized by ultrasonication in lysis buffer (8 M urea, 10 mM dithiothreitol [DTT], 50 mM NAM, 3 μ M tryptic soy agar, and 0.1% protease inhibitor cocktail) and centrifuged at $20,000 \times g$ for 10 min to remove the debris. The protein then was precipitated with cold 15% TCA for 2 h at -20°C and centrifuged at 4°C for 10 min, and the supernatant was discarded. After washing with cold acetone three times, the protein was redissolved in buffer (8 M urea, 100 mM triethylammonium bicarbonate [TEAB], pH 8.0) and the protein concentration determined with a 2-D Quant kit (GE Healthcare, PA, USA) according to the manufacturer's instructions.

For trypsin digestion, the protein solution was first reduced with 10 mM DTT for 1 h at 37°C and alkylated with 20 mM indole-3-acetic acid (IAA) for 45 min at room temperature in darkness. The protein sample then was diluted by adding 100 mM TEAB to a final urea concentration of less than 2 M. Finally, trypsin was added at a 1:50 trypsin-to-protein mass ratio for the first digestion overnight and a 1:100 trypsin-to-protein mass ratio for a second 4-h digestion.

After trypsin digestion, the peptide was desalted using a Strata X C₁₈ SPE column (Phenomenex, CA, USA) and then was vacuum dried. The peptide was reconstituted in 1 M TEAB and processed according to the manufacturer's protocol for the 6-plex TMT kit (Thermo Fisher Scientific, MA, USA). To enrich the acetylated peptides, tryptic peptides were dissolved in NETN buffer (100 mM NaCl, 1 mM EDTA, 50 mM Tris-HCl, 0.5% NP-40, pH 8.0) and then were incubated with prewashed anti-acetyl lysine antibody-conjugated agarose beads (PTM-104; PTM Biolabs, Hangzhou, China) at 4°C overnight with gentle shaking. The beads were washed four times with NETN buffer and twice with double-distilled water. The bound peptides were eluted from the beads with 0.1% trifluoroacetic acid. The eluted fractions were combined

and vacuum dried. The resulting peptides were cleaned by using C₁₈ ZipTip pipette tips (Millipore, MA, USA) according to the manufacturer's instructions.

For LC-MS/MS analysis, peptides were dissolved in 0.1% formic acid and then were directly loaded onto a reversed-phase precolumn (Acclaim PepMap 100; Thermo, MA, USA). Peptide separation was performed using a reversed-phase analytical column (Acclaim PepMap RSLC; Thermo, MA, USA). Gradient elution was performed by increasing solvent B (0.1% formic acid in 98% acetonitrile) from 7% to 25% over 40 min, 25% to 40% over 12 min, 40% to 80% over 4 min, and then holding at 80% for the last 4 min, all at a constant flow rate of 400 nL/min on an EASY-nLC 1000 ultraperformance liquid chromatography (UPLC) system. The peptides were subjected to nanospray ionization followed by tandem mass spectrometry (MS/MS) using a Q Exactive Orbitrap mass spectrometer (Thermo, MA, USA) coupled with an ultraperformance liquid chromatography system. Intact peptides were detected in the Orbitrap at a resolution of 70,000. Peptides were selected for MS/MS using the Normalized Collision Energy (NCE) setting of 28; ion fragments were detected in the Orbitrap at a resolution of 17,500. A data-dependent procedure that alternated between one MS scan followed by 20 MS/MS scans was applied for the top 20 precursor ions above a threshold ion count of 1E4 in the MS survey scan with 15.0-s dynamic exclusion. The electrospray voltage applied was 2.0 kV. Automatic gain control (AGC) was used to prevent overfilling of the Orbitrap; 5×10^4 ions were accumulated for the generation of MS/MS spectra. For MS scans, the *m/z* scan range was 350 to 1,800. The fixed first mass was set at 100 *m/z*.

The resulting MS/MS data were processed using the MaxQuant software package with an integrated Andromeda search engine (v.1.5.2.8). Tandem mass spectra were searched against the Swiss-Prot *Mus musculus* database concatenated with the reverse decoy database. Trypsin/P was specified as the cleavage enzyme, allowing up to 4 missing cleavages, 5 modifications per peptide, and 5 charges. The mass error was set to 10 ppm for precursor ions and 0.02 Da for fragment ions. Cysteine carbamidomethylation was specified as a fixed modification, and methionine oxidation, lysine acetylation, and protein N-terminal acetylation were specified as variable modifications. False discovery rate (FDR) thresholds for proteins, peptides, and modification sites were specified at 1%. The minimum peptide length was set at 7. TMT-6plex was selected as the quantification method. All other parameters in MaxQuant were set to default values.

LC-MS analysis. The brain tissues (60 mg) were extracted in 1 ml of cold water-acetonitrile-isopropanol (1:2:2, vol/vol/vol) and vortexed before ultrasonication for 30 min twice on ice. The supernatant of the samples (after centrifugation at 13,000 $\times g$, 4°C, 15 min) was then speed vacuum dried for 4 h. Next, 50% acetonitrile was added to resuspend the lyophilized powder, followed by centrifugation at 14,000 $\times g$ for 20 min at 4°C to obtain the supernatant for metabolite analysis with an Agilent 1290 Infinity LC high-performance liquid chromatography system coupled to a 5500 QTRAP mass spectrometer.

For LC-MS analysis, the samples were separated using an Agilent 1290 Infinity LC UPLC system. The mobile phase consisted of a 10 mM ammonium acetate aqueous solution (liquid A) and acetonitrile (liquid B). The sample was placed in an automatic sampler at 4°C, the column temperature was 45°C, the flow rate was 300 liters/min, and the sample volume was 2 μ L. The gradient of the relevant liquid phase was set as the following: from 0 to 18 min, liquid B changed linearly from 90% to 40%; from 18 min to 18.1 min, liquid B changed linearly from 40% to 90%; liquid B then was maintained at 90% from 18.1 min to 23 min. A quality control sample was set for a certain number of experimental samples at every interval in the sample queue to test and evaluate the stability and repeatability of the system. A standard mixture of energy metabolites was used in the sample cohort for chromatographic retention time correction. Mass spectrometry analysis was performed using a 5500 QTRAP mass spectrometer (AB SCIEX, MA, USA) in anion mode. The 5500 QTRAP ESI source conditions were set up as the following: source temperature, 450°C; ion source gas 1, 45°C; ion source gas 2, 45°C; curtain gas, 30°C; and ion spray voltage floating, 4,500 V. MRM mode was used to detect the ion pairs to be measured.

Multiquant analysis was used to extract the chromatographic peak area and retention time. Standard energy metabolites were used to correct the retention time for metabolite identification.

Western blotting. Brain tissues or cultured cells were lysed in radioimmunoprecipitation assay (RIPA) buffer, and the protein concentrations were determined using a bicinchoninic acid protein assay kit (Beyotime, Shanghai, China). Equal quantities of total protein were resolved by 12% SDS-PAGE. For Western blotting, gels were transferred to polyvinylidene difluoride membranes (Bio-Rad, CA, USA). The membranes were blocked with 5% nonfat milk followed by incubation with a primary antibody and the corresponding HRP-conjugated secondary antibody. The blots were then visualized with ECL reagent (Beyotime, Shanghai, China) and detected using an Amersham Imager 600 enhanced chemiluminescence (ECL) analysis system (GE, MA, USA).

Immunoprecipitation. Brain tissues were homogenized with ultrasonication and centrifuged at 12,000 rpm for 10 min at 4°C. The supernatants were collected and incubated with anti-GAPDH, anti-PDH1 α , or anti-MDH1 rabbit polyclonal antibodies for 2 h at 4°C. Protein A/G beads were then added, and samples were rotated overnight at 4°C. Samples were centrifuged at 5,000 rpm for 1 min at 4°C, and the supernatants were discarded. The beads were washed three times with cold lysis buffer, suspended in loading buffer, placed in a boiling water bath for 10 min, and then subjected to SDS-PAGE followed by immunoblot analysis.

Analysis of metabolic enzyme activity. The activity of HK, GAPDH, LDH, PDH, CS, IDH, SDH, and MDH in brain tissues infected with different RABVs was detected according to the manufacturer's instructions (Solarbio, Beijing, China).

OAA treatment. Because OAA is easily decarboxylated to pyruvate, the pH of OAA solutions becomes more alkaline over time. We prepared OAA solution by dissolving OAA in PBS and adjusted the pH to 7.0 with NaOH immediately before use. For animal treatment, a 1-g/kg/day OAA solution was prepared by suspending 0.5 g of OAA in 10 ml of PBS with the pH adjusted to 7.0. The vehicle-treated group

TABLE 1 Primers used for qPCR

Primer	Sequence (5' to 3')
GLUT1-F	CAGTTCGGCTATAACACTGGTG
GLUT1-R	GCCCCGACAGAGAAGATG
β -Actin-F	GGCTGTATCCCTCCATCG
β -Actin-R	CCAGTTGGTAACAATGCCATGT
TNF α -F	CCCTCACACTCAGATCATCTTCT
TNF α -R	GCTACGACGTGGGCTACAG
CCL2-F	TTAAAAACCTGGATCGGAACCAA
CCL2-R	GCATTAGCTTCAGATTTACGGGT
CXCL10-F	CCAAGTGTGCCGTCATTTTC
CXCL10-R	GGCTCGCAGGGATGATTTCAA
vRNA-F	CCTCGTCGTAGAGTTGACA
vRNA-R	GAGGAATCTTCGGGAAAGG

received PBS. After i.c. inoculation with CVS, C57/BL6 mice were intraperitoneally injected with PBS or OAA solution for 7 days. For each mouse, the volume received by intraperitoneal injection was the body weight (g) \times 0.02 ml.

qPCR. RNA was extracted with TRIzol reagent (Thermo, MA, USA) and reverse transcribed with HiScript II Q RT supermix (Vazyme, Nanjing, China) to obtain cDNA. The quantitative real-time PCR volume was 20 μ l, and the following cycling parameters were used: 95°C for 5 min, followed by 40 cycles at 95°C for 15 s and 60°C for 30 s. The transcript levels of genomic RNA and targeted genes were calculated relative to the levels of β -actin using the formula $2^{-(CT(\beta\text{-actin}) - CT(\text{Target Gene}))}$. The primers used in this study are listed in Table 1.

Isolation of leukocytes in the CNS. Leukocytes from the brains of CVS-infected mice were isolated and analyzed as follows. Mice were intracardially perfused with PBS. Brains were removed and digested with 2 μ g/ μ l collagenase D (number 51657124; Roche, Germany) and 1 μ g/ μ l DNase I (number 52779120; Roche, Germany) in Hanks balanced salt solution for 1 h to disperse the tissue into single-cell suspension. Cells were then separated by discontinuous Percoll gradient (70/30%) centrifugation for 25 min (650 \times g at room temperature, without brake). After being washed once with Hanks balanced salt solution, cells were stained for CD45 (30-F11; number 553079), B220 (RA3-6B2; number 561881), CD11b (M1/70; number 557397), Ly6G (1A8; number 560602), CD11c (N418; number 565872) (BD Pharmingen, CA, USA), CD45 (QA17A26; number 157611), CD3 (17A2; number 100203) (BioLegend, CA, USA), and TMEM119 (number 2281213; Invitrogen, CA, USA) with directly conjugated antibodies. Data collection and analysis were performed using a BD FACSVerser flow cytometer (BD Biosciences, CA, USA) and FlowJo software (TreeStar, CA, USA).

Immunohistochemistry. Six-week-old female C57BL/6 mice were i.c. inoculated with 200 FFU of CVS-, DRV-, or mock-infected DMEM. At 7 dpi, the mice were anesthetized with ketamine-xylazine and perfused by intracardiac injection with PBS, followed by 4% neutral paraformaldehyde, as described previously. The brain tissues were collected and fixed with 4% neutral paraformaldehyde for 48 h before being paraffin embedded and sliced for immunohistochemistry analysis. After being heated at 70°C for 10 min, the sliced sections were dipped in CitriSolv solvent (Servicebio, Wuhan, China) and dried. The sections were incubated with proteinase K in 10 mM Tris-HCl (pH 7.4 to 8.0) for 10 min and rinsed three times with PBS. A CD45 primary antibody and a secondary antibody were used for immunological reactions. Finally, diaminobenzidine was added for color development.

Statistical analysis. Bubble chart and Venn diagram analyses were performed using the OmicShare tool (<https://www.omicshare.com/>), a free online platform for data analysis. Heat map representation of the lysine acetylation level and energy metabolites was performed using Microsoft Excel software (MS Office 2019). The immunohistochemistry graphs were analyzed with the IHC profile plugins of ImageJ according to a previous report (47). The quantities and ratios of differentially expressed proteins and comparisons of biological tests were analyzed and represented by using GraphPad Prism (version 8.0) software (GraphPad, San Diego, CA, USA). Student's *t* test was performed to analyze the significant differences between the two groups. One-way analysis of variance (ANOVA) was performed to analyze the significant differences between the three groups (*, *P* < 0.05; **, *P* < 0.01; ***, *P* < 0.001).

Data availability. The MS/MS raw data have been deposited in ProteomeXchange and are accessible through accession number PXD029404 (<http://proteomecentral.proteomexchange.org/cgi/GetDataset?ID=PX029404>).

ACKNOWLEDGMENTS

This research was supported by the National Natural Science Foundation of China (31872451 to L.Z.; 31720103917 and 31872452 to Z.F.).

REFERENCES

- O'Sullivan A, Willoughby RE, Mishchuk D, Alcarraz B, Cabezas-Sanchez C, Condori RE, David D, Encarnacion R, Fatteh N, Fernandez J, Franka R, Hedderwick S, McCaughy C, Ondrush J, Paez-Martinez A, Rupprecht C, Velasco-Villa A, Slupsky CM. 2013. Metabolomics of cerebrospinal fluid from humans treated for rabies. *J Proteome Res* 12:481–490. <https://doi.org/10.1021/pr3009176>.

2. Li XQ, Sarmiento L, Fu ZF. 2005. Degeneration of neuronal processes after infection with pathogenic, but not attenuated, rabies viruses. *J Virol* 79: 10063–10068. <https://doi.org/10.1128/JVI.79.15.10063-10068.2005>.
3. Scott CA, Rossiter JP, Andrew RD, Jackson AC. 2008. Structural abnormalities in neurons are sufficient to explain the clinical disease and fatal outcome of experimental rabies in yellow fluorescent protein-expressing transgenic mice. *J Virol* 82:513–521. <https://doi.org/10.1128/JVI.01677-07>.
4. Dhingra V, Li X, Liu Y, Fu ZF. 2007. Proteomic profiling reveals that rabies virus infection results in differential expression of host proteins involved in ion homeostasis and synaptic physiology in the central nervous system. *J Neurovirol* 13:107–117. <https://doi.org/10.1080/13550280601178226>.
5. Farahat F, Zandi F, Khalaj V, Biglari P, Fayaz A, Vaziri B. 2013. Proteomics analysis of human brain tissue infected by street rabies virus. *Mol Biol Rep* 40:6443–6450. <https://doi.org/10.1007/s11033-013-2759-0>.
6. Thanomsridetchai N, Singtho N, Tepsunmethanon V, Shuangshoti S, Wacharapluesadee S, Sinchaikul S, Chen ST, Hemachudha T, Thongboonkerd V. 2011. Comprehensive proteome analysis of hippocampus, brainstem, and spinal cord from paralytic and furious dogs naturally infected with rabies. *J Proteome Res* 10:4911–4924. <https://doi.org/10.1021/pr200276u>.
7. Zandi F, Eslami N, Torkashvand F, Fayaz A, Khalaj V, Vaziri B. 2013. Expression changes of cytoskeletal associated proteins in proteomic profiling of neuroblastoma cells infected with different strains of rabies virus. *J Med Virol* 85:336–347. <https://doi.org/10.1002/jmv.23458>.
8. Schutsky K, Portocarrero C, Hooper DC, Dietzschold B, Faber M. 2014. Limited brain metabolism changes differentiate between the progression and clearance of rabies virus. *PLoS One* 9:e87180. <https://doi.org/10.1371/journal.pone.0087180>.
9. Venugopal AK, Ghantasala SS, Selvan LD, Mahadevan A, Renuse S, Kumar P, Pawar H, Sahasrabhuddhe NA, Suja MS, Ramachandra YL, Prasad TS, Madhusudhana SN, Hc H, Chaerkady R, Satishchandra P, Pandey A, Shankar SK. 2013. Quantitative proteomics for identifying biomarkers for rabies. *Clin Proteomics* 10:3. <https://doi.org/10.1186/1559-0275-10-3>.
10. Zhao S, Xu W, Jiang W, Yu W, Lin Y, Zhang T, Yao J, Zhou L, Zeng Y, Li H, Li Y, Shi J, An W, Hancock SM, He F, Qin L, Chin J, Yang P, Chen X, Lei Q, Xiong Y, Guan KL. 2010. Regulation of cellular metabolism by protein lysine acetylation. *Science* 327:1000–1004. <https://doi.org/10.1126/science.1179689>.
11. Guan KL, Xiong Y. 2011. Regulation of intermediary metabolism by protein acetylation. *Trends Biochem Sci* 36:108–116. <https://doi.org/10.1016/j.tibs.2010.09.003>.
12. Lin SJ, Guarente L. 2003. Nicotinamide adenine dinucleotide, a metabolic regulator of transcription, longevity and disease. *Curr Opin Cell Biol* 15: 241–246. [https://doi.org/10.1016/s0955-0674\(03\)00006-1](https://doi.org/10.1016/s0955-0674(03)00006-1).
13. Yang H, Yang T, Baur JA, Perez E, Matsui T, Carmona JJ, Lamming DW, Souza-Pinto NC, Bohr VA, Rosenzweig A, de Cabo R, Sauve AA, Sinclair DA. 2007. Nutrient-sensitive mitochondrial NAD⁺ levels dictate cell survival. *Cell* 130:1095–1107. <https://doi.org/10.1016/j.cell.2007.07.035>.
14. Wilkins HM, Harris JL, Carl SM, Lezi E, Lu J, Eva Selfridge J, Roy N, Hutfles L, Koppel S, Morris J, Burns JM, Michaelis ML, Michaelis EK, Brooks WM, Swerdlow RH. 2014. Oxaloacetate activates brain mitochondrial biogenesis, enhances the insulin pathway, reduces inflammation and stimulates neurogenesis. *Hum Mol Genet* 23:6528–6541. <https://doi.org/10.1093/hmg/ddu371>.
15. Campos F, Sobrino T, Ramos-Cabrera P, Argibay B, Agulla J, Perez-Mato M, Rodriguez-Gonzalez R, Brea D, Castillo J. 2011. Neuroprotection by glutamate oxaloacetate transaminase in ischemic stroke: an experimental study. *J Cereb Blood Flow Metab* 31:1378–1386. <https://doi.org/10.1038/jcbfm.2011.3>.
16. Yamamoto HA, Mohanan PV. 2003. Effect of alpha-ketoglutarate and oxaloacetate on brain mitochondrial DNA damage and seizures induced by kainic acid in mice. *Toxicol Lett* 143:115–122. [https://doi.org/10.1016/s0378-4274\(03\)00114-0](https://doi.org/10.1016/s0378-4274(03)00114-0).
17. Wilkins HM, Koppel S, Carl SM, Ramanujan S, Weidling I, Michaelis ML, Michaelis EK, Swerdlow RH. 2016. Oxaloacetate enhances neuronal cell bioenergetic fluxes and infrastructure. *J Neurochem* 137:76–87. <https://doi.org/10.1111/jnc.13545>.
18. Nagy D, Marosi M, Kis Z, Farkas T, Rakos G, Vecsei L, Teichberg VI, Toldi J. 2009. Oxaloacetate decreases the infarct size and attenuates the reduction in evoked responses after photothrombotic focal ischemia in the rat cortex. *Cell Mol Neurobiol* 29:827–835. <https://doi.org/10.1007/s10571-009-9364-8>.
19. Kuang Y, Han X, Xu M, Wang Y, Zhao Y, Yang Q. 2018. Oxaloacetate ameliorates chemical liver injury via oxidative stress reduction and enhancement of bioenergetic fluxes. *Int J Mol Sci* 19:1626. <https://doi.org/10.3390/ijms19061626>.
20. Tian B, Zhou M, Yang Y, Yu L, Luo Z, Tian D, Wang K, Cui M, Chen H, Fu ZF, Zhao L. 2017. Lab-attenuated rabies virus causes abortive infection and induces cytokine expression in astrocytes by activating mitochondrial antiviral-signaling protein signaling pathway. *Front Immunol* 8:2011. <https://doi.org/10.3389/fimmu.2017.02011>.
21. Li T, Liu M, Feng X, Wang Z, Das I, Xu Y, Zhou X, Sun Y, Guan KL, Xiong Y, Lei QY. 2014. Glyceraldehyde-3-phosphate dehydrogenase is activated by lysine 254 acetylation in response to glucose signal. *J Biol Chem* 289: 3775–3785. <https://doi.org/10.1074/jbc.M113.531640>.
22. Yu W, Lin Y, Yao J, Huang W, Lei Q, Xiong Y, Zhao S, Guan KL. 2009. Lysine 88 acetylation negatively regulates ornithine carbamoyltransferase activity in response to nutrient signals. *J Biol Chem* 284:13669–13675. <https://doi.org/10.1074/jbc.M901921200>.
23. Narita T, Weinert BT, Choudhary C. 2019. Functions and mechanisms of non-histone protein acetylation. *Nat Rev Mol Cell Biol* 20:156–174. <https://doi.org/10.1038/s41580-018-0081-3>.
24. Huang J, Zhang Y, Huang Y, Gnanadurai CW, Zhou M, Zhao L, Fu ZF. 2017. The ectodomain of rabies virus glycoprotein determines dendritic cell activation. *Antiviral Res* 141:1–6. <https://doi.org/10.1016/j.antiviral.2017.01.022>.
25. Potratz M, Zaack L, Christen M, Te Kamp V, Klein A, Nolden T, Freuling CM, Müller T, Finke S. 2020. Astrocyte infection during rabies encephalitis depends on the virus strain and infection route as demonstrated by novel quantitative 3D analysis of cell tropism. *Cells* 9:412. <https://doi.org/10.3390/cells9020412>.
26. Wang ZW, Sarmiento L, Wang Y, Li XQ, Dhingra V, Tsegai T, Jiang B, Fu ZF. 2005. Attenuated rabies virus activates, while pathogenic rabies virus evades, the host innate immune responses in the central nervous system. *J Virol* 79: 12554–12565. <https://doi.org/10.1128/JVI.79.19.12554-12565.2005>.
27. Pösel C, Uri A, Schulz I, Boltze J, Weise G, Wagner DC. 2014. Flow cytometric characterization of brain dendritic cell subsets after murine stroke. *Exp Transl Stroke Med* 6:11. <https://doi.org/10.1186/2040-7378-6-11>.
28. Lartigue L, Faustin B. 2013. Mitochondria: metabolic regulators of innate immune responses to pathogens and cell stress. *Int J Biochem Cell Biol* 45:2052–2056. <https://doi.org/10.1016/j.biocel.2013.06.014>.
29. Mills EL, Kelly B, O'Neill LAJ. 2017. Mitochondria are the powerhouses of immunity. *Nat Immunol* 18:488–498. <https://doi.org/10.1038/ni.3704>.
30. Conti C, Superti F, Divizia M, Pana A, Orsi N. 1990. Effect of inhibitors of cytoplasmic structures and functions on rabies virus infection in vitro. *Comp Immunol Microbiol Infect Dis* 13:137–146. [https://doi.org/10.1016/0147-9571\(90\)90276-y](https://doi.org/10.1016/0147-9571(90)90276-y).
31. Koepsell H. 2020. Glucose transporters in brain in health and disease. *Pflugers Arch Eur J Physiol* 472:1299–1343. <https://doi.org/10.1007/s00424-020-02441-x>.
32. Maher F, Vannucci SJ, Simpson IA. 1994. Glucose transporter proteins in brain. *FASEB J* 8:1003–1011. <https://doi.org/10.1096/fasebj.8.13.7926364>.
33. Aebersold R, Agar JN, Amster J, Baker MS, Bertozzi CR, Boja ES, Costello CE, Cravatt BF, Fenselau C, Garcia BA, Ge Y, Gunawardena J, Hendrickson RC, Hergenrother PJ, Huber CG, Ivanov AR, Jensen ON, Jewett MC, Kelleher NL, Kiessling LL, Krogan NJ, Larsen MR, Loo JA, Ogorzalek Loo RR, Lundberg E, MacCoss MJ, Mallick P, Mootha VK, Mrksich M, Muir TW, Patrie SM, Pesavento JJ, Pitteri SJ, Rodriguez H, Saghatelian A, Sandoval W, Schluter H, Sechi S, Slavoff SA, Smith LM, Snyder MP, Thomas PM, Uhlen M, Van Eyk JE, Vidal M, Walt DR, White FM, Williams ER, Wohlschläger T, Wysocki VH, et al. 2018. How many human proteoforms are there? *Nat Chem Biol* 14:206–214. <https://doi.org/10.1038/nchembio.2576>.
34. Schwer B, Eckersdorff M, Li Y, Silva JC, Fermin D, Kurtev MV, Giallourakis C, Comb MJ, Alt FW, Lombard DB. 2009. Calorie restriction alters mitochondrial protein acetylation. *Aging Cell* 8:604–606. <https://doi.org/10.1111/j.1474-9726.2009.00503.x>.
35. Ventura M, Mateo F, Serratos J, Salaet I, Carujo S, Bachs O, Pujol MJ. 2010. Nuclear translocation of glyceraldehyde-3-phosphate dehydrogenase is regulated by acetylation. *Int J Biochem Cell Biol* 42:1672–1680. <https://doi.org/10.1016/j.biocel.2010.06.014>.
36. Swerdlow RH, Bothwell R, Hutfles L, Burns JM, Reed GA. 2016. Tolerability and pharmacokinetics of oxaloacetate 100 mg capsules in Alzheimer's subjects. *BBA Clin* 5:120–123. <https://doi.org/10.1016/j.bbaci.2016.03.005>.
37. Zlotnik A, Sineelnikov I, Gruenbaum BF, Gruenbaum SE, Dubilet H, Dubilet E, Leibowitz A, Ohayon S, Regev A, Boyko M, Shapira Y, Teichberg VI. 2012. Effect of glutamate and blood glutamate scavengers oxaloacetate and pyruvate on neurological outcome and pathohistology of the hippocampus after traumatic brain injury in rats. *Anesthesiology* 116:73–83. <https://doi.org/10.1097/ALN.0b013e31823d7731>.
38. Kammouni W, Wood H, Jackson AC. 2017. Lyssavirus phosphoproteins increase mitochondrial complex I activity and levels of reactive oxygen species. *J Neurovirol* 23:756–762. <https://doi.org/10.1007/s13365-017-0550-z>.

39. Kammouni W, Wood H, Saleh A, Appolinario CM, Fernyhough P, Jackson AC. 2015. Rabies virus phosphoprotein interacts with mitochondrial complex I and induces mitochondrial dysfunction and oxidative stress. *J Neurovirol* 21:370–382. <https://doi.org/10.1007/s13365-015-0320-8>.
40. Kammouni W, Wood H, Jackson AC. 2017. Serine residues at positions 162 and 166 of the rabies virus phosphoprotein are critical for the induction of oxidative stress in rabies virus infection. *J Neurovirol* 23:358–368. <https://doi.org/10.1007/s13365-016-0506-8>.
41. Liu SQ, Gao X, Xie Y, Wang Q, Zhu WY. 2020. Rabies viruses of different virulence regulates inflammatory responses both in vivo and in vitro via MAPK and NF-kappaB pathway. *Mol Immunol* 125:70–82. <https://doi.org/10.1016/j.molimm.2020.06.011>.
42. Liu SQ, Xie Y, Gao X, Wang Q, Zhu WY. 2020. Inflammatory response and MAPK and NF-kappaB pathway activation induced by natural street rabies virus infection in the brain tissues of dogs and humans. *Virology* 17: 157. <https://doi.org/10.1186/s12985-020-01429-4>.
43. Zhang Y, Wu Q, Zhou M, Luo Z, Lv L, Pei J, Wang C, Chai B, Sui B, Huang F, Fu ZF, Zhao L. 2020. Composition of the murine gut microbiome impacts humoral immunity induced by rabies vaccines. *Clin Transl Med* 10:e161. <https://doi.org/10.1002/ctm2.161>.
44. Sui B, Chen D, Liu W, Wu Q, Tian B, Li Y, Hou J, Liu S, Xie J, Jiang H, Luo Z, Lv L, Huang F, Li R, Zhang C, Tian Y, Cui M, Zhou M, Chen H, Fu ZF, Zhang Y, Zhao L. 2020. A novel antiviral lncRNA, EDAL, shields a T309 O-GlcNAcylation site to promote EZH2 lysosomal degradation. *Genome Biol* 21:228. <https://doi.org/10.1186/s13059-020-02150-9>.
45. Yu F, Zhang G, Xiao S, Fang L, Xu G, Yan J, Chen H, Fu ZF. 2012. Complete genome sequence of a street rabies virus isolated from a rabid dog in China. *J Virol* 86:10890–10891. <https://doi.org/10.1128/JVI.01775-12>.
46. Sui B, Chen D, Liu W, Tian B, Lv L, Pei J, Wu Q, Zhou M, Fu ZF, Zhang Y, Zhao L. 7 December 2020. Comparison of lncRNA and mRNA expression in mouse brains infected by a wild-type and a lab-attenuated rabies lyssavirus. *J Gen Virol* <https://doi.org/10.1099/jgv.0.001538>.
47. Varghese F, Bukhari AB, Malhotra R, De A. 2014. IHC Profiler: an open source plugin for the quantitative evaluation and automated scoring of immunohistochemistry images of human tissue samples. *PLoS One* 9: e96801. <https://doi.org/10.1371/journal.pone.0096801>.